

Electrostatic Levitator for High Temperature Containerless Materials Processing

Won-Kyu Rhim, Sang K. Chung, Daniel Barber, Kin F. Man, Gary Gutt,
Aaron Rulison[†], and R. Erik Spjut^{††}

Jet 1 Propulsion Laboratory, California Institute of Technology
48(10 Oak Grove Drive, Pasadena, CA 91109

ABSTRACT

This paper discusses recent developments in high temperature electrostatic levitation technology for containerless processing of metals and alloys. This is the first demonstration of the electrostatic levitation technology which can levitate metals and alloys (2 - 4 mm diameter spheres) in vacuum and the superheating-undercooling-recalescence cycles can be repeated while maintaining good positioning stability. The electrostatic levitator (ESL) has several important advantages over the electromagnetic levitator (EML). The most important advantage is the wide range of sample temperature which can be achieved without affecting the sample levitation. This paper also describes the general architecture of the levitator, electrode design, position control hardware and software, sample heating, charging, and preparation methods, and the operational procedure. Particular emphasis is given to sample charging by photoelectric and thermionic emission. While this ESL is more oriented toward ground-based operation, an extension to microgravity applications is also addressed briefly. The system performance was demonstrated by showing a superheating-undercooling-recalescence cycle in a zirconium sample ($T_m = 2128$ K). This levitator, when fully matured, will be a valuable tool both in Earth-based and space-based laboratories for the studies of thermophysical properties of undercooled liquids and nucleation kinetics, the creation of metastable phases, and access to a wide range of materials with novel properties,

[†] NASA- NRC Resident Research Associate

^{††} Department of Engineering, Harvey Mudd College, Claremont, CA

1. INTRODUCTION

The capability of containerless materials processing is important for the studies of thermophysical properties of undercooled liquid states, nucleation kinetics, and for the production of various metastable phases in different materials with novel properties. The electrostatic levitator described in this paper provides the capability of superheating, undercooling, and solidifying metals and alloys in a clean (contactless and high vacuum) and quiescent environment. This levitator is an extension of the one previously described¹ in which sample levitation was limited to low density materials at ambient conditions.

Suspension of charged particles by electrostatic forces has a rather long history. To our knowledge, however, none of these past applications have addressed high temperature materials processing. The advantages of the present high-temperature high-vacuum electrostatic levitator (ESL) are apparent when it is compared with the electromagnetic levitator (EML)², the only alternative technique having similar capabilities: (i) The ESL can accommodate a broad range of materials, including metals, semiconductors and insulators, since maintaining a sufficient surface charge on the sample is the only requirement to generate a levitation force, in contrast, an EML relies on eddy currents induced in a conducting sample by an applied rf magnetic field. Mutual interaction between the eddy currents and the applied field results in a levitation force. Materials that the EML can levitate are, therefore, limited primarily to electrical conductors. (ii) In an ESL, sample heating and levitation do not interfere with each other so that the sample temperature can be varied over a wide range; whereas the electromagnetic field in an EML is intrinsically coupled to sample heating, which limits the lowest temperature it can attain for a given sample density. (iii) The ESL, through employment of feedback control, provides quiescent positioning during sample processing; whereas a molten sample levitated by an EML is subjected to strong internal flow which may cause severe shape distortion, prevents accurate temperature measurements, and perhaps causes premature nucleation, therefore preventing deeper undercooling. (iv) The ESL provides a more open view; whereas the levitation and heating coils in an EML are closely wound around the levitated sample, severely restricting access to the diagnostic instruments. However, one major drawback of the ESL is that it requires either a high

vacuum or a high pressure environment in order for a high electric field to be applied without causing gas breakdown.

We describe in this paper an electrostatic levitator which has demonstrated for the first time the capability to process materials at high temperature in a dean environment. A brief review of the basic principle of an electrostatic levitator is given, followed by a description of the general architecture of the levitator, electrode design, position control hardware and software, sample heating, charging, and the operational procedure. The system performance is demonstrated using zirconium samples which melt at 2128 K. We conclude with a discussion on some intrinsic problems and aspects that need to be improved in the future, and also point out how some of the difficulties we face in ground-based laboratories can be overcome in the micro-gravity environment of space.

11. PRINCIPLE OF ELECTROSTATIC LEVITATION

In electrostatic levitation the positioning of a charged sample is achieved through the application of feedback-controlled electrostatic fields that are generated by a set of appropriately positioned electrodes around the sample. Since a three-dimensional electrostatic potential minimum does not exist (Earnshaw's theorem³), electrostatic sample positioning is only possible with an actively controlled applied electric field. In our system this was accomplished using a feedback-control whereby any deviation in sample position from a preset position was automatically corrected.

Fig.1 shows a schematic diagram of an electrostatic levitator with one-dimensional control capability. This system employs a single-axis position control along the vertical direction to overcome the gravitational acceleration, g . The vertical position information from a position detector is compared to a preset z -coordinate to generate an error signal which is processed by a computer to generate a control signal according to a feedback algorithm. The control signal is amplified and applied to the top electrode to maintain the sample at the preset position. The force-balance equation for levitation when the sample is positioned at the center of a pair of infinite parallel electrodes is given by:

$$mg = Q_s V/L, \quad (1)$$

where m is the mass of the sample carrying a charge Q_s , and V is the voltage difference between the two electrodes separated by a distance L . For $Q_s = 0.69 \times 10^{-9}$ C, $m = 140$ mg, and $L = 10$ mm, V is approximately -10 kV.

As explained in reference (4), the electrode arrangement shown in Fig. 1 provides a two-dimensional potential well in the horizontal direction when it is operated in the presence of a gravitational force on earth, but such a potential well does not exist and it would require a different electrode arrangement and control method in the microgravity environment of space.

III. POSITION CONTROL HARDWARE

A schematic diagram of the present high temperature/high vacuum electrostatic levitator is shown in Fig. 2. The electrode assembly is housed in a cylindrical vacuum chamber and all the necessary equipment for levitation, heating, and diagnostics are located around the chamber. The 1 ft³ stainless steel chamber can be evacuated to an ultimate vacuum of 5×10^{-8} Torr by a vibration-free magnetically suspended turbo-molecular pump.

A schematic diagram of the electrode assembly shown in Fig. 3 is located at the center of the chamber. The basic difference between this and the electrodes shown in Fig. 1 is the addition of two pairs of side electrodes surrounding the bottom electrode. Damping voltages applied on these side electrodes prevent sample oscillation in the lateral directions. Without the side electrodes the lateral position instability would introduce uncertainties into the diagnostic measurements.

Two orthogonal HeNe lasers (30 mW each) together with two position detectors provide the 3-dimensional position information which is used by the microcomputer to generate a feedback signal. A Macintosh IIx computer and 12 bit A/D, D/A cards were used for data acquisition and position control. The computer is equipped with a Motorola 50 MHz 68030 microprocessor and 68882 floating point math coprocessor. The 12 bit A/D and D/A cards from National Instruments fit into the Nubus inside the computer. The three position signals (produced by the two

orthogonally -positioned detectors) are fed into the computer through an A/D card, and after going through the control routine the three output signals are sent to the high voltage amplifiers through a D/A card. The position sensitive detectors (PSD) camera by HAMAMATSU are commercially available. This type of detector is normally used for sensing a bright image on a dark background. In our system, however, due to the xenon lamp light (used for heating) which brightly illuminates the chamber and the sample, we had to use it in reversed mode (dark sample on a bright- background). This was accomplished by adding a collimated HeNe laser beam in the background and attaching a matching narrow band filter in front of the detector to pass only the laser wavelength while stopping others coming from the xenon lamp. The computer converts the detector output to the actual sample position.

Sample heating is provided by a 1 -kilowatt UV-rich high-pressure xenon arc lamp (1 I.C). The radiation produced by the bulb is roughly collimated into a 2 inch beam by a parabolic reflector at the back of the bulb housing. The beam is then focused by a 3 inch focal length fused quartz lens into a small spot in order to maximize the light flux on the sample. Since the beam originates from a finite discharge gap between the anode and the cathode and not from a point source, the focused spot size could not be reduced to less than 5 mm. Fused quartz was used in order to transmit the UV component of the xenon beam for sample charging via the photoelectric effect, (Sample charging by UV will be described in section V.) A fused quartz mirror, 3 inches both in diameter and in radius of curvature, is placed opposite the lens. This mirror collects most of the xenon light beam that misses the sample. The temperature of a 2.5 mm diameter zirconium sphere could be varied from room temperature to 2270 K by adjusting the iris in front of the xenon lamp. Without the mirror, the maximum temperature could not exceed 1750 K.

The sample temperature was measured using a home-built single-color pyrometer which was constructed and calibrated according to the prescription provided by Hofmeister et al.⁵. The pyrometer collects the radiative power emitted by a well-defined area on the sample surface into a certain solid angle and over a small wavelength range (10 nm band width at 658 nm wavelength). The collected power can be converted to sample temperature through Planck's equation for the spectral distribution of

emissive power if the pyrometer output corresponding to one temperature is known, typically at the sample melting point. For zirconium, the rapid increase in temperature at the melting point as a result of recalescence provides an easily recognized reference point, allowing the temperature to be calculated *a posteriori* for the entire undercooling experiment. Data acquisition was by a Macintosh 11 computer with a National Instruments A/D converter. The driving software automatically recognizes the reference temperature, T_{ref} , by searching for the rapid increase in the pyrometer output associated with recalescence. It then calculates the temperature for the entire experiment and provides a plot of temperature versus time. The percentage of undercooling and other important parameters are also computed and displayed.

A close-up view of the sample was videotaped during the experiments using a camera with a telephoto lens.

IV. THE POSITION CONTROL SOFTWARE

The software is divided into two groups: FOREGROUND and BACKGROUND. The foreground task consists of the servo control and the data collection that require synchronized operations with highest priority. The background task consists of a user interface, a display such as a keyboard and mouse response, and graphics, which are given secondary priority. Data files can also be created and saved onto the hard drive through the background mode. These two modes of operation are made possible by the use of the interrupt request capability of the Macintosh computer. When an interrupt signal is issued (from an external programmable pulse generator) the computer sets aside background routines, stores its present state of the registers into a memory, and launches the foreground routine. During the foreground routine, the position information is collected from an A/D, the control algorithm is then launched, a proper servo control value is sent out through a D/A, and a single frame of data is collected in a specified memory buffer. After the foreground routine is successfully executed, the computer recaptures its previous register values and continues with its background task. This process is set into a continuous loop with an interrupt frequency of 480 Hz.

a **Servo Control**

The vertical axis servo control utilizes the commonly used PID (Proportional, Integral, Derivative) algorithm⁶. Its z-output value at the i-th cycle, O_i , has the following form:

$$O_i = PG \times e_i + IG \times \sum_{i=0}^i e_i + DG \times (e_i - e_{i-1}), \quad (2)$$

where

$e_i = sp - z_i$, error signal at the i-th loop

z_i = current vertical position

sp = set-position

PG = proportional gain

IG = integral gain

DG = derivative gain.

Since the horizontal plane has a passive potential minimum it does not normally require an active feedback control. However, in vacuum, there is no gas medium to damp out horizontal oscillations, so we used a horizontal clamping control consisting of two sets of side electrodes. The lateral clamping was controlled by the following simple algorithm:

$$O_{ij} = DG \times (e_{ij} - e_{i-1,j}), \quad (3)$$

where

$e_{ij} = sp_j - p_{ij}$, error signal for a single loop

$j = x$ or y component of position

p_{ij} = x or y position at the i-th cycle.

The vertical control is executed in every loop whereas the horizontal control can be executed at a rate ten times slower. The actual stability of the sample has been found to depend strongly on the vibration of the system originating from floor vibrations. A stability better than 20 μm was achieved for a 3 mm sample with a specific density of 8, carrying a constant charge,

b. User Interface

The user interface consists of a keyboard/mouse input and a graphics display. The keyboard/mouse is used for entering servo and other necessary parameters for proper data acquisition. It can, therefore, interrupt the loop at any time, although the servo-loop has a higher priority. The graphics display consists of sample positions, control voltage outputs and temperature readings (Fig. 4). The programs were written in 'C' language except the interrupt handler routine which was written in assembly code,

V. SAMPLE CHARGING

Sample charging is a critical part of electrostatic positioning. The amount of charge on the sample surface determines the positioning force that can be imparted onto the sample with a given electrostatic field. In order for the electrostatic positioning technique to be employed, the physical processes that allow charges to accumulate on the sample had to be identified. This involved studying sample charging methods which are applicable to different sample materials in different processing environments. Three charging methods that are relevant during different phases of processing have been employed: inductive, photoelectric and thermionic charging.

Inductive charging is employed for sample launching and levitation at the beginning of each experiment prior to the use of the other charging mechanisms. In inductive charging, surface charge on the sample increases as the top electrode potential increases until electrical contact with the bottom electrode is broken and the sample levitated. In order to make the charge polarity consistent with that induced by the other charging methods, a positive charge was induced by applying negative voltages on the top electrode. The initial sample charge will remain unchanged only in the absence of any discharging ions which may be produced by the sample and the surrounding electrodes under strong xenon irradiation. When more than one charging mechanisms are acting simultaneously, sample charging becomes a dynamic process. Photoelectric charging tends to maintain a sufficient charge even in the presence of neutralizing ions. Once the sample temperature exceeds approximately 1200 °C, the more powerful thermionic charging

mechanism eventually dominates the photoelectric charging, enhancing the sample charge.

Photoelectric emission arises as a result of electron excitation by radiation, usually within a depth that the radiation can penetrate. Emission of a photoelectrically excited electron can occur only if it possesses sufficient energy to reach the surface and overcome the work function. The amount of sample charging depends on the photoelectric yield, which is the number of emitted electrons per absorbed photon. For most metals, emission is more effective in the UV range (less than 400 nm). At photon energies of several eV above threshold, the photoelectric yield from metals is of the order of 10^{-4} electrons per photon. At photon energies 5-20 eV above threshold (corresponding to wavelengths in the vacuum UV region), the yield increases to a maximum of about 0.1 electrons per photon which is attributed to emissions from the bulk material deep inside the surface layer⁷. Since maintaining a high positive charge on the sample is the objective, it is desirable to encourage high electron emission by the sample while discouraging electron emission by the electrodes. This can be accomplished by selecting electrode materials having a higher work function than the sample material,

The rate of thermal electron emission from a heated solid follows the Richardson - Dushman equation:

$$J(\phi_s, T) = AT^2 \exp\left(-\frac{\phi_s}{kT}\right), \quad (4)$$

where $A = 120 \text{ Amp/cm}^2\text{K}^2$, k is the Boltzmann constant, ' T ' is the absolute temperature, and ϕ_s is the effective work function. J is a rapidly increasing function of temperature and thermionic emission is the dominant charging mechanism when the sample temperature exceeds 1200°C , even in the presence of various discharging electrons and ions.

a. Numerical Analysis of Inductive Charging

A general-purpose three-dimensional computer model was created to determine the potential, charge, and force distributions on a sample in an electrostatic levitator. Since an analytical solution of this system with arbitrary sample and electrode geometries is impractical, this model uses a

numerical finite-difference approach. The potential and charge distributions are obtained using a Multigrid Method solver⁸ and the forces on the sample are derived from these distributions. This model allows us to evaluate and optimize different electrode configurations for the levitator.

The relationships between the parameters (e.g. sample size, position, density, charge, forces, and electrode potentials) that are obtained from this model are shown in Figs. 6 - 9 to give some insights into this system. In all of the examples the levitator consists of circular top and bottom disk electrodes, separated by 10 mm and with the top electrode connected to a HV amplifier while the bottom electrode is grounded. The sample was assumed to be spherical (see Fig. 5(a)). Without going into the details (a detailed description of this model will be published elsewhere), we will simply present a few exemplary cases to elucidate the general relationship between sample size, position, density, charge, and electrode voltage.

Fig. 6 shows the top electrode potential as a function of sample diameter at the moment of launch. The corresponding induced charge on the sample is shown in Fig. 7. Fig. 8 shows the z-component of the force on the sample as a function of the sample position for the case of fixed sample charge and a constant top electrode voltage. The variation in force as a function of position is due to the image charges on the electrodes induced by the charged sample. The force increases as the sample moves up, showing the need for an active feedback system to control the levitation voltage. Fig. 9 shows the radial restoring force on the sample as a function of sample displacement from the center, which is also primarily due to image charges.

b. A Model for Sample Charging by Photoelectric and Thermionic Emission

When a cold sample is launched with initial charge Q_s , it requires a levitation voltage given approximately by Eq. (1). However, V is subjected to change as Q_s changes. In fact this is what happens when the sample is irradiated by UV or when the sample temperature is high enough to cause thermionic emission. When the sample is heated by a focused xenon lamp beam, the UV component ejects electrons not only from the sample but also from surrounding materials as a result of reflection and scattering. The equilibrium charge of a levitated sample is established through the balance of electrical currents flowing between the sample and electrodes. These

include photoelectric and thermionic currents, as well as currents resulting from ionization of gases and other volatile materials. Consider the case in which the sample has reached a steady-state temperature and is positioned between the top electrode (at a negative potential V) and the bottom electrode (grounded). A current I_p (taken to be positive for electron leaving the sample) flowing from the sample to the bottom electrode may be expressed by

$$I_p = -\alpha_s V_s [Y_s f_s F + \delta_s + J(\phi_s, T_s)] \equiv -V_s / R_p \quad (5)$$

where α_s is a geometrical factor relating relative sizes and shapes of the sample and electrode to the amount of current that can be extracted from the sample at a given sample potential V_s , Y_s is the sample's photoelectric yield, f_s is the fraction of the xenon lamp flux which has photon energy larger than the sample's work function, F is the total xenon lamp flux falling on the sample, δ_s represents positive ionization of gas molecules on the sample's lower surface via surface ionization $J(\phi_s, T_s)$ is the thermionic current as defined in Eq. (4), and R_p is defined as the equivalent resistance. Similarly, the current flowing from the top electrode to the sample (taken to be positive for electrons leaving the top electrode) is

$$I_u = \alpha_u (V_s - V) (Y_u r_{su} s_{su} f_u F + \delta_u) \equiv (V_s - V) / R_u \quad (6)$$

where α_u is a geometrical factor relating the sample and electrode shapes to the amount of current which originates from the top electrode at potential V and reaches the sample, Y_u is the top electrode's photoelectric yield, r_{su} is the sample reflectivity, s_{su} is the fraction of the reflected beam falling on the top electrode, f_u is the fraction of the xenon lamp output which has energy higher than the top electrode work function, δ_u represents positive ionization of gas molecules on the sample's lower surface, and R_u is defined as the equivalent resistance. The present situation may be represented by an equivalent circuit shown in Fig. 5(b) where C_u and C_p are the mutual capacitances between the sample and the

top and the bottom electrodes, respectively. Therefore, the sample charge is given by

$$\begin{aligned} Q_s &= Q_p - Q_u \\ &= C_p V_s - C_u (V - V_s) \\ &= (C_p + C_u) V_s - C_u V. \end{aligned} \quad (7)$$

where Q_p is the charge on C_p , and Q_u is the charge on C_u .

If the top electrode voltage jumps from an initial steady state value V_0 to a final value V_f , then the solutions of the equivalent circuit are given by

$$V_s(t) - V_{s0} = [V_s(\infty) - V_{s0}] [1 - \exp(-t/\tau)], \quad (8)$$

where

$$V_s(\infty) = V_f \frac{\alpha}{1 + \alpha}, \quad (9)$$

$$\tau = \frac{(C_p + C_u) R_p}{1 + \alpha}, \quad (10)$$

with

$$\alpha \equiv R_p/R_u = \frac{\alpha_u (Y_u r_s s_{su} f_u F + \delta_u)}{\alpha_s [Y_s f_s F + \delta_s + J(\phi_s, T_s)]} \quad (11)$$

where Eq. (11) results from Eqns. (5) and (6). The solution for the sample charge, $Q_s(t)$, takes the same form as Eq. (8) with the same τ given by Eq. (10):

$$Q_s(t) - Q_{s0} = (Q_s(\infty) - Q_{s0}) [1 - \exp(-t/\tau)], \quad (12)$$

Where

$$Q_s(\infty) = V_f \frac{C_p + \alpha C_u}{1 + \alpha}. \quad (13)$$

Since V_{s0} and Q_{s0} are also steady state values their expressions are given by Eqns. (9) and (13), respectively, with V_0 replacing V_f .

If a spherical sample is midway between the electrodes, then $C_p \approx C_u \equiv C$, and C will be proportional to the sample size. Assuming $V_{s0} = 0$ so that $Q_{s0} = 0$, we have

$$V_s(\infty) = V_f \frac{\alpha}{1 + \alpha}, \quad (14)$$

$$Q_s(\infty) = -V_f C \frac{1 - \alpha}{1 + \alpha}. \quad (15)$$

From Eqns. (12) and (13), the force exerted on the sample is:

$$F_{es}(t) = -\frac{V_f^2 C(1 - \alpha)}{1 + \alpha} [1 - \exp(-t/\tau)], \quad (16)$$

and from Eq. (10),

$$\tau = \frac{2CR_p}{1 + \alpha}. \quad (17)$$

From these equations the following observations can be made:

(i) Since α is defined as a positive number in Eq. (11), the maximum positive sample charge cannot exceed $-V_f C$ and it can completely disappear when $\alpha = 1$. Dependence of $Q_s(\infty)$ and $V_s(\infty)$ on α can be seen more clearly in Fig. 10. This means that, in order to maintain a sufficient charge for levitation, one must control the parameters in Eq. (11) so that α is sufficiently small.

(ii) Since the sample charge is linearly dependent on V_f , $F_{es}(\infty)$ should show quadratic dependence on V_f as Eq. (16). This was experimentally verified as shown in Fig. 11. The force exerted on the sample in a UV rich environment was measured using a dynamic balance as a function of the electrode voltage. Of course, according to Eq. (16), the parabola appearing in Fig. 11 is determined by α , I , and C .

(iii) in order to achieve a fast response time, according to Eq. (17), CR_p should decrease, that is, since C is fixed for a given sample, R_p should decrease. This may be accomplished (Eq. (5)) by increasing the lamp flux F , and eventually by increasing $J(\phi_s, T_s)$ at higher temperatures. This trend was verified experimentally, again using the dynamic balance, as shown in Fig. 12. When the sample reached a steady state under a certain UV flux, a -10 kV step was applied to the electrode and the force imparted on the sample was recorded. As Fig. 12 shows, the basic trend is in accordance with Eq. (16).

(iv) If the sample is levitated using a top electrode voltage, V_f , then, from Eqns. (1) and (15), one obtains the sample charge and the required levitation voltage:

$$Q_s(\infty)^2 = -mgI C \frac{1 - \alpha}{1 + \alpha}, \quad (18)$$

and,

$$V_f^2 = \frac{mgl}{C} \frac{1 + \alpha}{1 - \alpha}. \quad (19)$$

Fig. 13 shows that the sample charge holds its largest value, \sqrt{mglC} , when $a = 0$, requiring the lowest electrode voltage, and the sample holds no charge if $a = 1$.

(v) We have seen from above examples the important role a plays for the sample charging, and for levitation we prefer $a \ll 1$. That is, from Eq. (11),

$$\alpha_u (Y_u r_s s_{su} f_u F + \delta_u) \ll \alpha_s [Y_s f_s F + \delta_s + J(\phi_s, T_s)].$$

In the thermionic temperature region where $J(\phi_s, T_s)$ dominates the other terms this inequality can be easily satisfied unless δ_u is equally high. In actual experiments we have observed more quiescent sample levitation with large sample charge as soon as the temperature exceeded about 1200°C . Therefore, the major concern for sample levitation may arise in the lower temperature range where J (ϕ_s, T_s) is insignificant. Since $0 \geq V_s > V_f$, a neutral atom ionized near the top surface of the sample donates an electron to the sample while the positive ion strikes the top-electrode producing electrons which will shower onto the sample, further decreasing the charge, i.e., increasing δ_u . On the other hand, a positive ion produced at the bottom surface of the sample cannot escape the sample due to the opposing field condition, thus ensuring $\delta_s \ll \delta_u$. Therefore, the issue is whether one can control the remaining parameters in such a way that:

$$\alpha_u (Y_u r_s s_{su} f_u F + \delta_u) \ll \alpha_s Y_s f_s F.$$

For a fixed xenon lamp flux, F , the condition $f_u \ll f_s$ can be achieved by choosing the work function of the top electrode larger than that of the sample, the condition $r_s \ll 1$ may be satisfied if the sample surface is not highly reflecting, and the situation $s_{su} \ll 1$ can be provided by making the solid angle extending to the electrode from the sample as small as possible. If the effect of δ_u cannot be easily overcome, the only remaining

remedy might be to reduce δ_u itself by allowing more gradual outgassing as the sample temperature is raised more slowly.

VI. SAMPLE PREPARATION

Clean, spherical samples of various metals were prepared for the undercooling experiments using a chemical etch and thermal outgassing treatment. The procedure was as follows: A rod made from a metal of interest was machined with a neck and bulb at one end. A chemical degrease and etch was applied to the rod to remove organic and inorganic surface impurities. The chemical treatment depended on its composition. For all metals the first step involved degreasing in trichloroethylene and in acetone each for 1 minute. The second step consisted of a chemical etch of the surface to remove the oxide layer and other inorganic surface impurities. The optimum acid etch solutions for many metals can be found in reference¹⁰.

After cleaning and etching, the rod was mounted vertically with the bulb facing down in a sample preparation chamber evacuated to -10^{-7} Torr. The bulb was heated by electron bombardment from a heated tungsten filament coil. About 4 kV potential was applied between the filament and the grounded rod. The bulb was kept just below its melting temperature for several hours to allow any adsorbed and absorbed gases to outgas. The heating was then increased until the bulb melted and formed a spherical pendant drop at the end of the rod. The heating was then terminated and the drop was allowed to cool and solidify. The chamber was purged with dry argon gas and the sample was clipped from the rod, ready for use in undercooling experiments. The size of the resulting sample could be easily controlled by the size of the initial bulb at the end of the rod.

VII. OPERATING PROCEDURE AND SYSTEM PERFORMANCE

The sample was positioned on the bottom electrode and the chamber evacuated to $\sim 10^{-8}$ Torr. The position control software was turned on and the appropriate set position and PG, DG, and IG gains were keyed in. A Trek 20 kV amplifier was used for the z-axis control and two Trek 10 kV amplifiers were used for the x- and y-axis damping. As soon as

the top electrode reached the threshold voltage the sample jumped away from the bottom electrode towards the set position. Minor adjustments to the gains and set point were then made to establish the most quiescent levitation conditions. The stability was typically better than 20 microns at this point.

The iris in front of the xenon lamp was then opened gradually while the levitation voltage was being monitored. Changes in the sample charge arc manifested by corresponding changes in Invitation voltage according to Eq. (1). If a substantial charge decrease occurred, the iris was adjusted so that the required control voltage lie within the range of the high voltage amplifiers (± 20 kV in this case). Ion production at the sample surface seemed to depend on the cleanliness of the sample surface and the degree of outgassing. Since the impurities outgassed during heating may be ionized and reduce the sample's charge, the impurities that arc volatile at each temperature arc removed through gradual heating of the sample and this process is continued until the desired final temperature is reached. As discussed above, since the sample charge is determined by α in the equivalent circuit (Fig. 5(b)), enough charge may be maintained by making α sufficiently small, i.e., by reducing R_p with increased photo-emission current while maintaining R_u relatively unchanged. This means that a top electrode having a higher work function than the sample is generally preferred. A 1 -inch diameter goldplated copper mirror performed well in the present system. As the sample charge changed during heating, the control gains were frequently adjusted in order to maintain the best position stability.

VIII. DEMONSTRATION OF AN UNDERCOOLING EXPERIMENT

Once the sample melted and reached the desired super-heated temperature, it was ready for an undercooling experiment. In a vacuum environment the change in internal energy of the sample is equal to the difference between the heat arriving from the xenon beam and that lost due to radiation:

$$\rho V C_p dT/dt = Q_{in} - A\sigma\epsilon_T(T^4 - T_b^4), \quad (20)$$

where p is the sample density, V is the volume, C_p is the heat capacity, Q_{in} is the heat due to the beam, A is the sample surface area, σ is the Stefan-Boltzmann constant, ϵ_T is the total hemispherical emissivity, T is the sample temperature, and T_b is the background temperature. This formulation assumes that the background acts as a blackbody, which is true in most cases where the sample chamber is much larger than the sample. The steady state temperature, T_f , is then given by:

$$T_f = (Q_{in}/A\sigma\epsilon + T_b^4)^{1/4}. \quad (21)$$

If the xenon beam is turned off, then $Q_{in} = 0$ in Eq. (20), and T_f will decay to T_b due to radiative cooling. Fig. 14 shows a molten drop of zirconium being levitated at $T_f = 2250$ K (120 K above its melting temperature) in the presence of a heating beam. The sample diameter was approximately 2.5 mm. The highlight spots seen on the sample disappeared when the beam was turned off. Fig. 15 shows a temperature vs. time curve of the same sample when the heating beam was suddenly removed at the sample temperature of 2250 K. Before the beam was removed the pyrometer was strongly influenced by reflected radiation, showing a high level of noise as seen at the beginning of the curve. Therefore, the temperature reading is inaccurate while the lamp is on. As soon as the beam is blocked the sample underwent radiative cooling according to Eq. (20) (with $Q_{in} = 0$) until recalescence occurred. Recalescence is marked by a sudden increase in temperature to its melting point as the sample releases its latent heat. The liquid-solid coexistence period lasted for approximately 0.3 seconds before the sample temperature decayed again. The data presented in this figure was obtained by digitizing the pyrometer output at 1 kHz.

Since $(T/T_b)^4 > 10^3$ during the undercooling period, one can integrate Eq. (20), assuming $T_b \approx 0$ and $\rho VC_p/3A\sigma\epsilon_T \approx \text{constant}$, to give:

$$t - t_o = (\rho VC_p / 3A\sigma\epsilon_T) (T_o^{-3} - q - s), \quad (22)$$

where T_o is the sample temperature at $t = t_o$. A plot of t vs. T^{-3} is shown in Fig. 16 confirming a linear relationship.

IX. SUMMARY AND DISCUSSION

A high-temperature/high-vacuum electrostatic levitator has been constructed for containerless materials processing. An undercooling experiment with a zirconium sample clearly demonstrates the ability of the system to levitate a dense material stably at high temperature. We have also demonstrated the control of temperature without affecting the position stability, and the open view of the sample for diagnostic measurements. These capabilities will enable a wide range of experiments, which were hitherto impossible, to be conducted on the ground.

We have described some of the basic principles and physical mechanisms involved in the high temperature electrostatic levitator operated in the presence of gravity. The basic PID feedback routine seems to be adequate for the position control despite the fact that the sample charge was subjected to a dynamic process. Rapid advancements in some commercial products, notably the high resolution position detector, the high speed micro-computer, the high voltage amplifiers, the vibration-free vacuum pumps, and the user friendly programming languages, have greatly improved the system performance and made the construction of a new system easier.

So far we have successfully melted and solidified numerous sample materials: In (157 °C), Sn (232 °C), Bi (271.44 °C), Pb (327 °C), In_{0.69}W_{0.31}Sb (492.5 °C), Al (670 °C), Ge (938 °C), Cu (1083 °C), Ni (1455 °C), and Zr (1855 °C), (melting temperatures are shown in parenthesis). In the case of zirconium we have completed more than 400 quantitative undercooling experiments. Results of these experiments will be published elsewhere. However, we have not yet demonstrated the capability to process non-conducting sample materials, an area which we plan to investigate in the near future. We have also limited the processing environment only to high vacuum which has the advantage of ensuring better sample cleanliness. However, for more volatile sample materials a gaseous environment may be more desirable. The heaviest sample that an electrostatic levitator can levitate will be limited by the breakdown voltage of the medium, but this problem will be alleviated in a reduced-g environment where the control voltage can be reduced by several orders of magnitude.

Numerical calculations of sample charges, launch voltages, and the levitation forces as functions of sample size and density give an important guideline for the initial 'cold' levitation. This analysis has revealed that sample densities as high as 20 can be levitated with a voltage of -20 kV, as long as the sample size does not exceed 2.5 mm in diameter. We were able to levitate a small gold sample to demonstrate this point.

The simple R-C circuit used to model the charge gain/loss behavior under the influence of photoelectric or thermionic emission may be an oversimplification. However, the present model has been very useful for identifying those physical mechanisms which affect the sample charge. Constructing a more realistic model will be possible as we gain more experience with the system. A systematic experimental investigation is being planned. One important practical lesson we have learned is that in order to conduct a successful experiment one must begin with a clean sample (with reduced volatile contents) and heat it slowly until it reaches the thermionic temperature.

The levitator described in this paper is primarily for Earth-based applications. It can, however, be readily converted for operation in a reduced-g environment. First we note that the sample charge produced by photoelectric and thermionic emissions is positive and proportional to the magnitude of the applied field, therefore, the control force is proportional to V^2 in magnitude and opposed to the applied field. The isotropic force environment of space leads to an electrode assembly having a tetrahedral symmetry with four spherical electrodes¹. As noted earlier the magnitude of the control force in space can be reduced by several orders of magnitude and it may be possible to operate in a gaseous environment. The design of a system specifically for space application is underway and will be described elsewhere.

X. ACKNOWLEDGMENTS

The authors would like to thank Dr. W. I. Hofmeister for his guidance in the construction of the silicon pyrometer and Dr. K. Ohsaka for providing us with the alloys used in the present work. This work was carried out at the Jet Propulsion Laboratory, California Institute of Technology, under contract with the National Aeronautics and Space Administration.

XI. REFERENCES

- 1, W. K. Rhim, M. Collender, M. T. Hlyson, W. T. Simms, and D. D. Elleman, Rev. Sci. Instrum. **56**, 307 (1985).
2. C. A. Hahs and R. J. Fox, Proc. 4th Int. Conf. on Exp. Methods for Microgravity Mat. Sci. Research, p23, Ed. R. A. Schiffman (1992).
- 3 , For Earnshaw's theorem, see for example S. A. Stratton, Electromagnetic Theory, (McGraw-Hill, New York, p 116,194 1.)
4. W. K. Rhim, S. K. Chung, E. H. Trinh, and D. D. Elleman, Proc. Mat. Res. Soc. 87, 329 (1 987).
5. W. F. Hofmeister, R. J. Bayuzick, and M. B. Robinson, Rev, Sci. Instrum. 61, 2220 (1990)0
6. J. A. Cadzow and H. R. Martnes, Discrete Time and Computer Control Sys_t cms (Prentice Hall, Englewood, NJ) (1970).
7. R. Gomer, Field Emission and Field ionization, Harvard University Press, Cambcidge, Massachusetts (1961).
8. Achi Brandt, Multigrid 'techniques: 1984 Guide, Lecture notes for the Computational Fluid Dynamics Lecture Series, Rhode-Saint-Genese, Belgium, 26-30, March (1984). W. I.. Briggs, A Multigrid Tutorial, Society for Industrial and Applied Mathematics, Philadelphia, PA (1987).
9. E. Ya. Zandberg, and N. I. Ionov, Soviet Phys. Uspehki, 67, 255 (1 959).
10. R. C. Snogren, Handbook of Surface Preparation, (Palmerton Pub. Co., Inc., New York) (1974),

FIGURE CAPTIONS

- Fig. 1. Schematic diagram of an electrostatic levitator in which the sample position is actively controlled only along the vertical direction. It relies on a two-dimensional potential well for centering in the lateral direction.
- Fig. 2. Schematic diagram of the high temperature-high vacuum electrostatic levitator designed for ground-based applications. 1 is the sample, 2 is the electrode assembly, 3 is the focusing lens, 4 is the spherical reflector, 5D and 6D are the position detectors, 5L and 6L are the He-Ne lasers, 7 is the 1-kW xenon lamp, 8 is the video-camera with a telephoto lens, and 9 is the pyrometer.
- Fig. 3. Schematic diagram of the electrode assembly (side and top views), where 1 is the sample, 2 is the top electrode, 3 is the bottom electrode, 4's are the side electrodes, and 5 is the hole which allows access to the sample storage system.
- Fig. 4. User interface display used in the present levitator. The cubical box represents the space between the electrodes in which the sample (the gray dot) moves in search of the set-point (the black dot) by feedback control. The status column displays the sample position, applied high voltages, and the sample temperature. The control parameter column shows the control parameter inputs. The sample position, the control voltage, and the sample temperature are also displayed in the form of oscillograms.
- Fig. 5. (a) Electrode and sample arrangements used in the numerical modeling of the initial 'cold' levitation. (b) The equivalent R-C circuit which was used to model the dynamic sample charging process under UV irradiation,
- Fig. 6. Top electrode voltage at the moment of launch versus sample diameter at three sample densities. Separation between the top and bottom electrodes is 10 mm.
- Fig. 7. Charge on the sample at the moment of launch versus sample diameter at three densities. Separation between the top and bottom electrodes is 10 mm,
- Fig. 8. Sample force in the z-axis versus sample position in the z-axis at different sample charge and top electrode voltages. Separation

between top and bottom electrodes is 8 mm and the sample diameter is 3 mm.

Fig. 9. Sample force in the x-axis versus sample position in the x-axis with a sample charge of 1.0 nC and a top electrode voltage of - 10 kV. Separation between top and bottom electrodes is 8 mm and the sample diameter is 3 mm,

Fig. 10. Sample charge and sample voltage versus α when a fixed voltage V_f is applied to the top electrode.

Fig. 11. The electrostatic force on the sample as a function of applied voltage on the top electrode.

Fig. 12. The transient behavior of the electrostatic force as a result of application of a -10 kV step at different UV flux and sample temperatures.

Fig. 13. Sample charge and corresponding levitation voltage versus α while the sample is levitated against the gravitational force.

Fig. 14. A molten zirconium sample being levitated at 2250 K.

Fig. 15. Temperature versus time as a superheated zirconium drop under goes radiative cooling.

Fig. 16. Time versus T^3 of the under-cooling segment (between 0.3 - 1.6 sec) shown in Fig. 15.

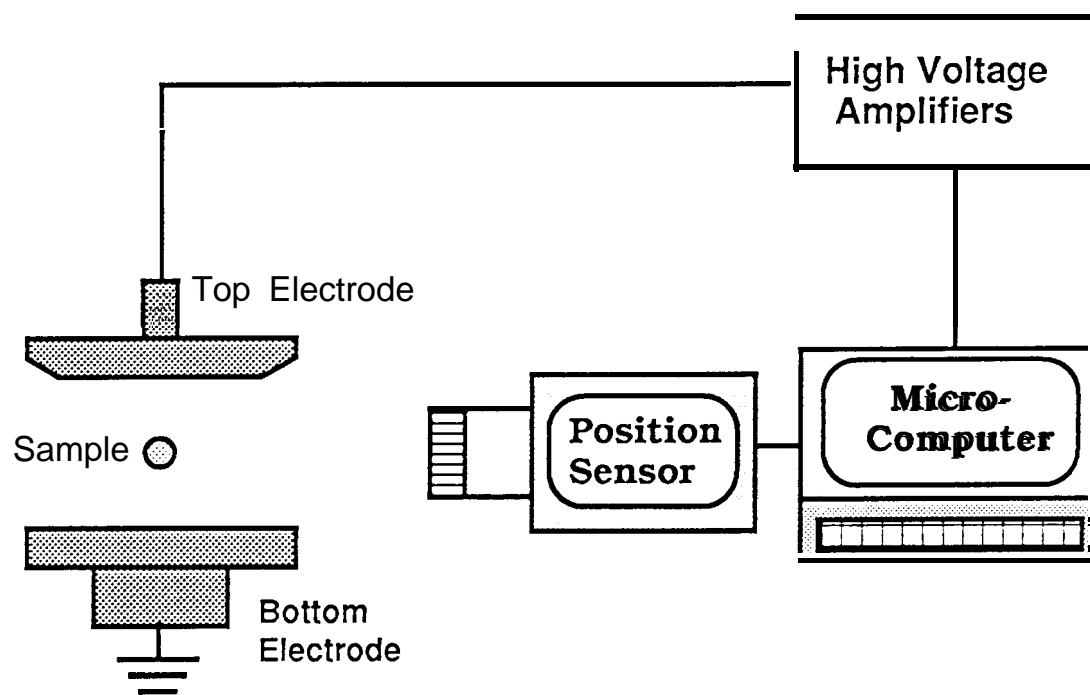


Fig 1

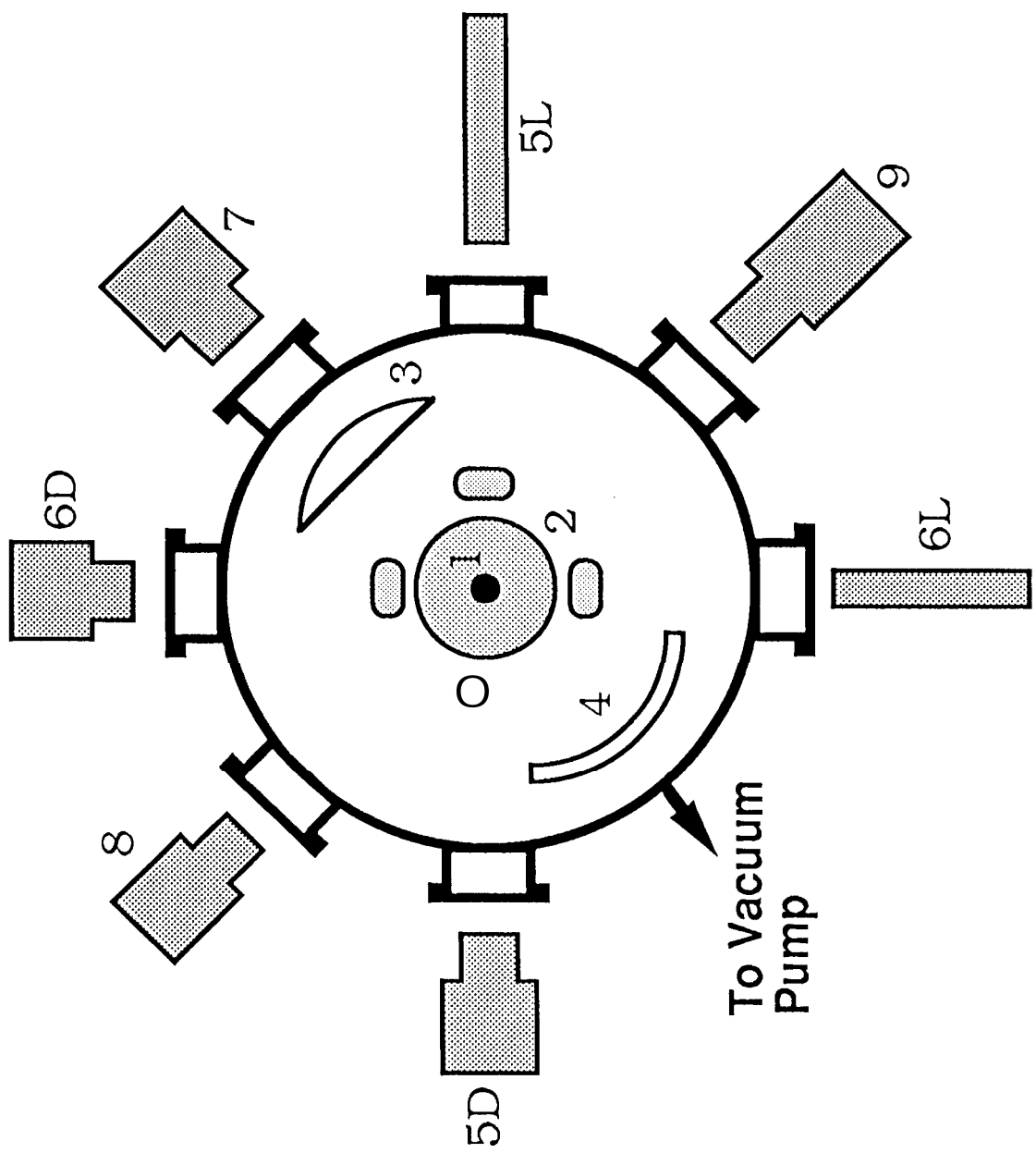


Fig 2

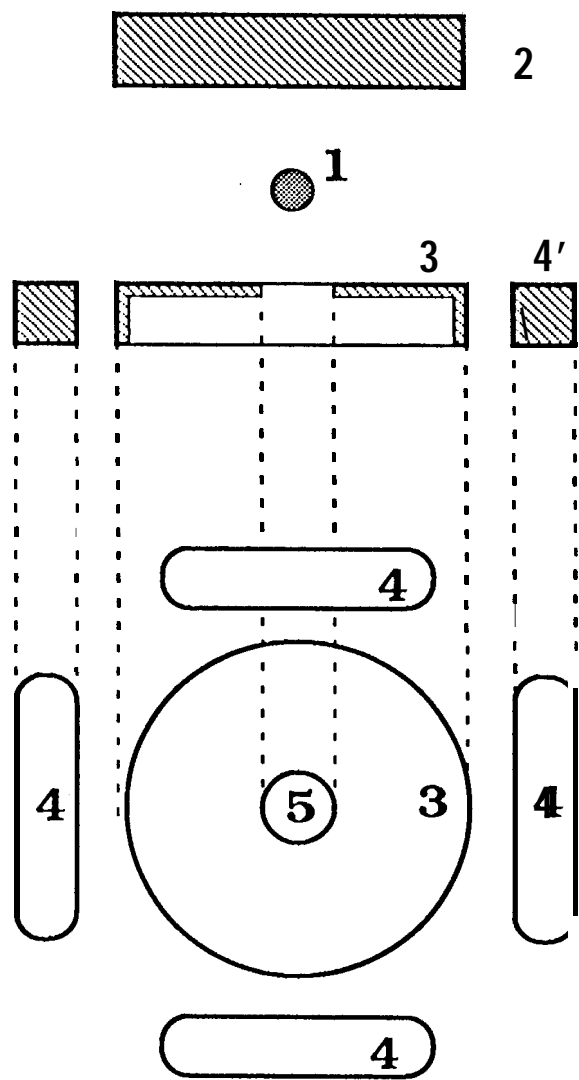
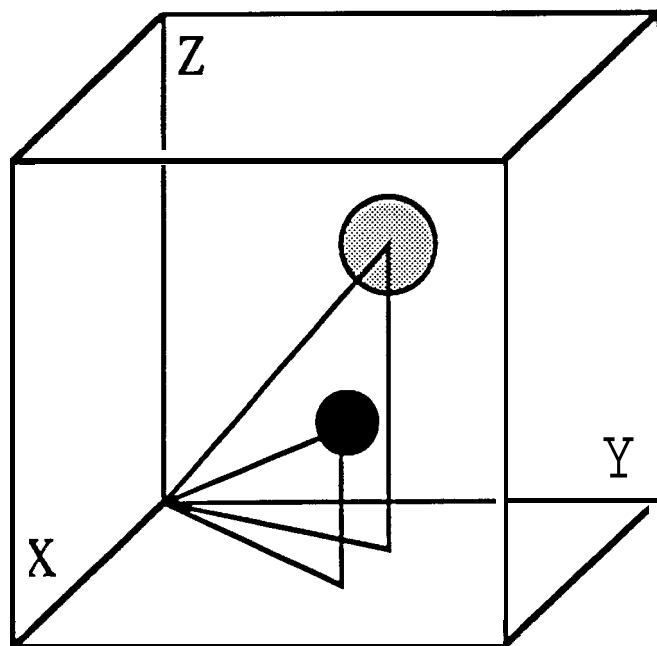


Fig 3



Frame Rate 480

Status

X	2040
Y	2052
Z	2021
HV 1	10.2 K
HV 2	0.2 K
HV 3	-1.2K
Temp	1230°

Control Parameters

PG	1200
IG	25
<input checked="" type="radio"/> DG	500
SDG	200
Setp	2021
<input type="checkbox"/> Fame rate	480

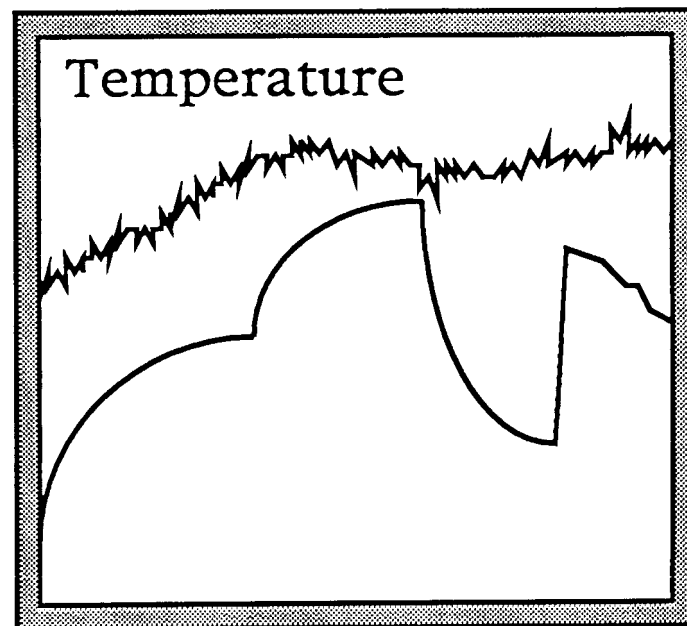
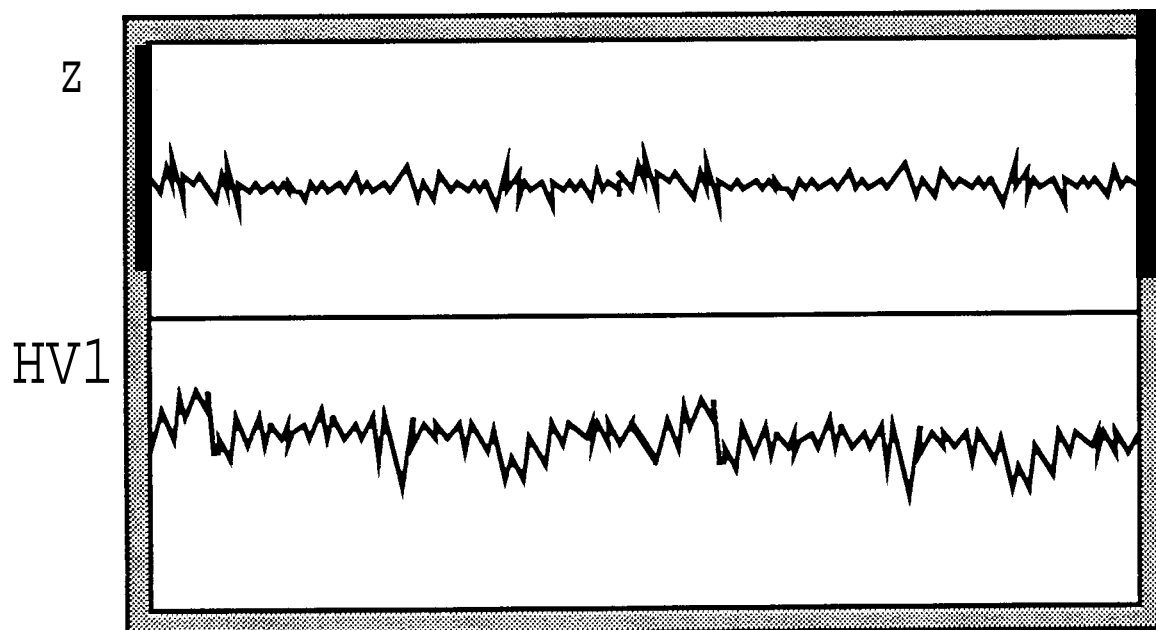


Fig. 4

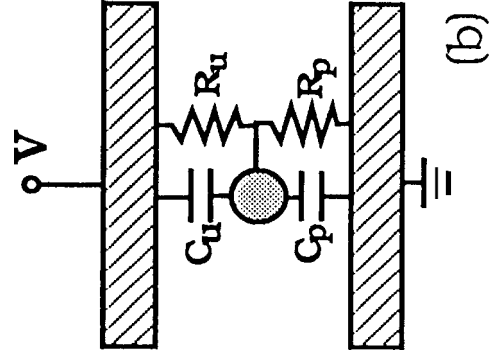
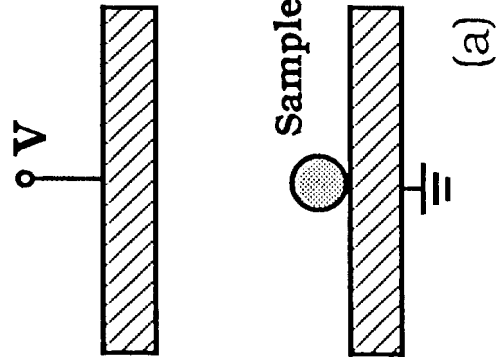


Fig. 5

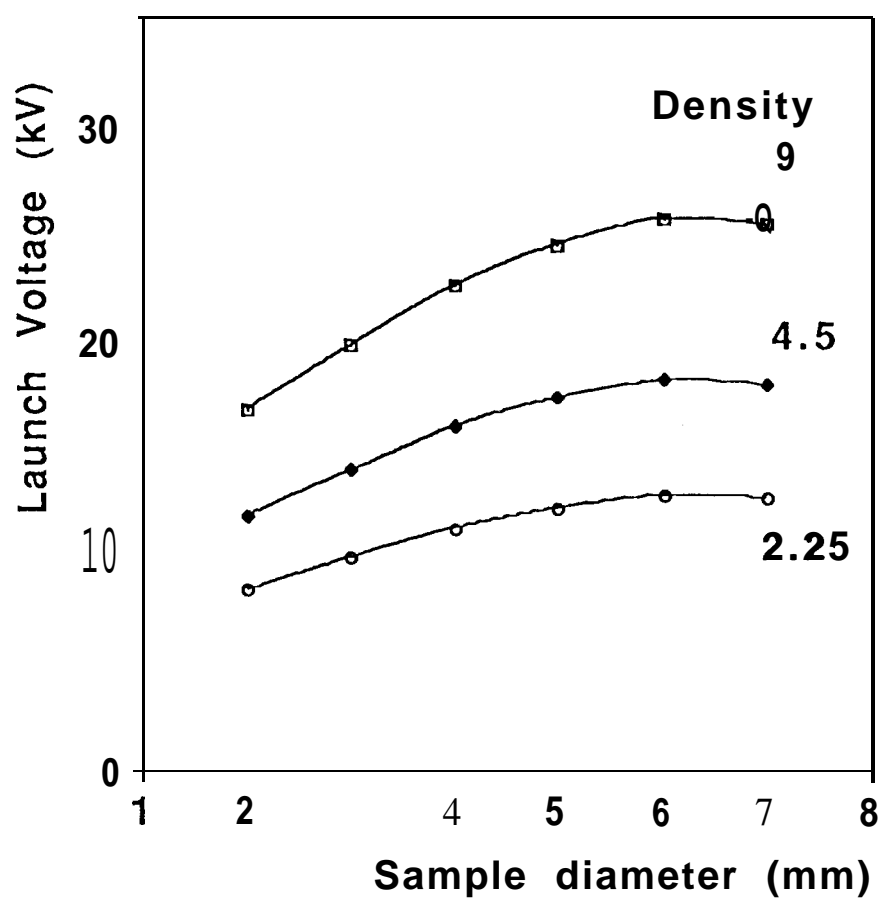


Fig. 6

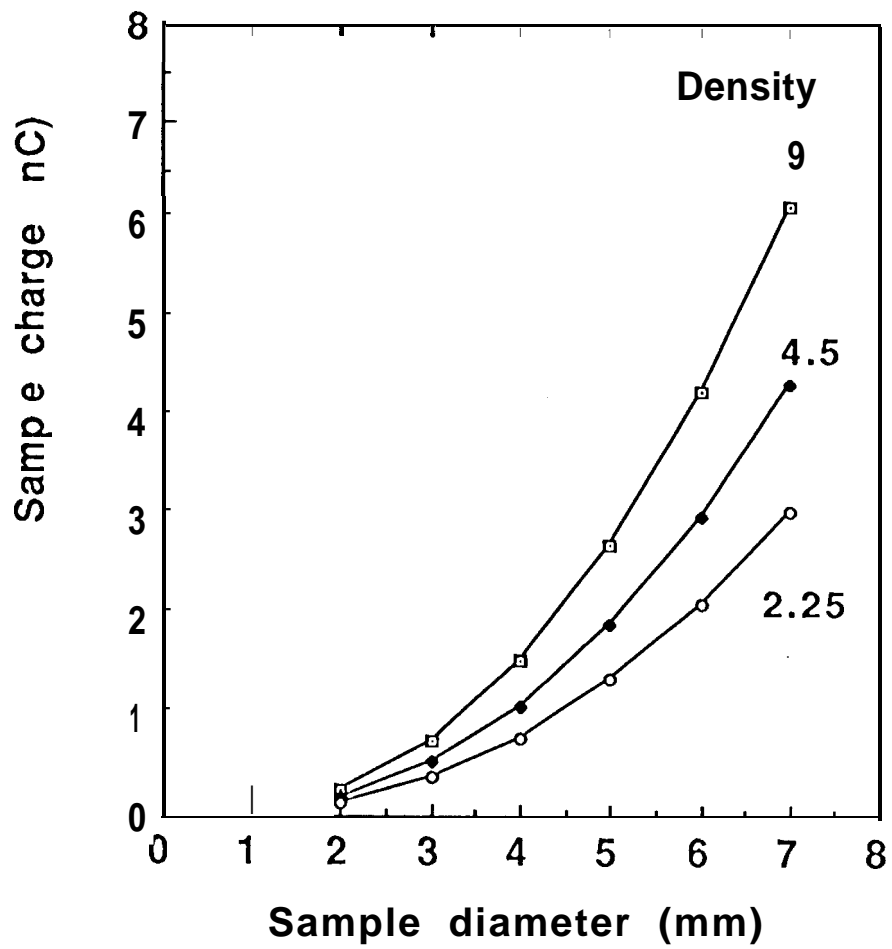


Fig. 7

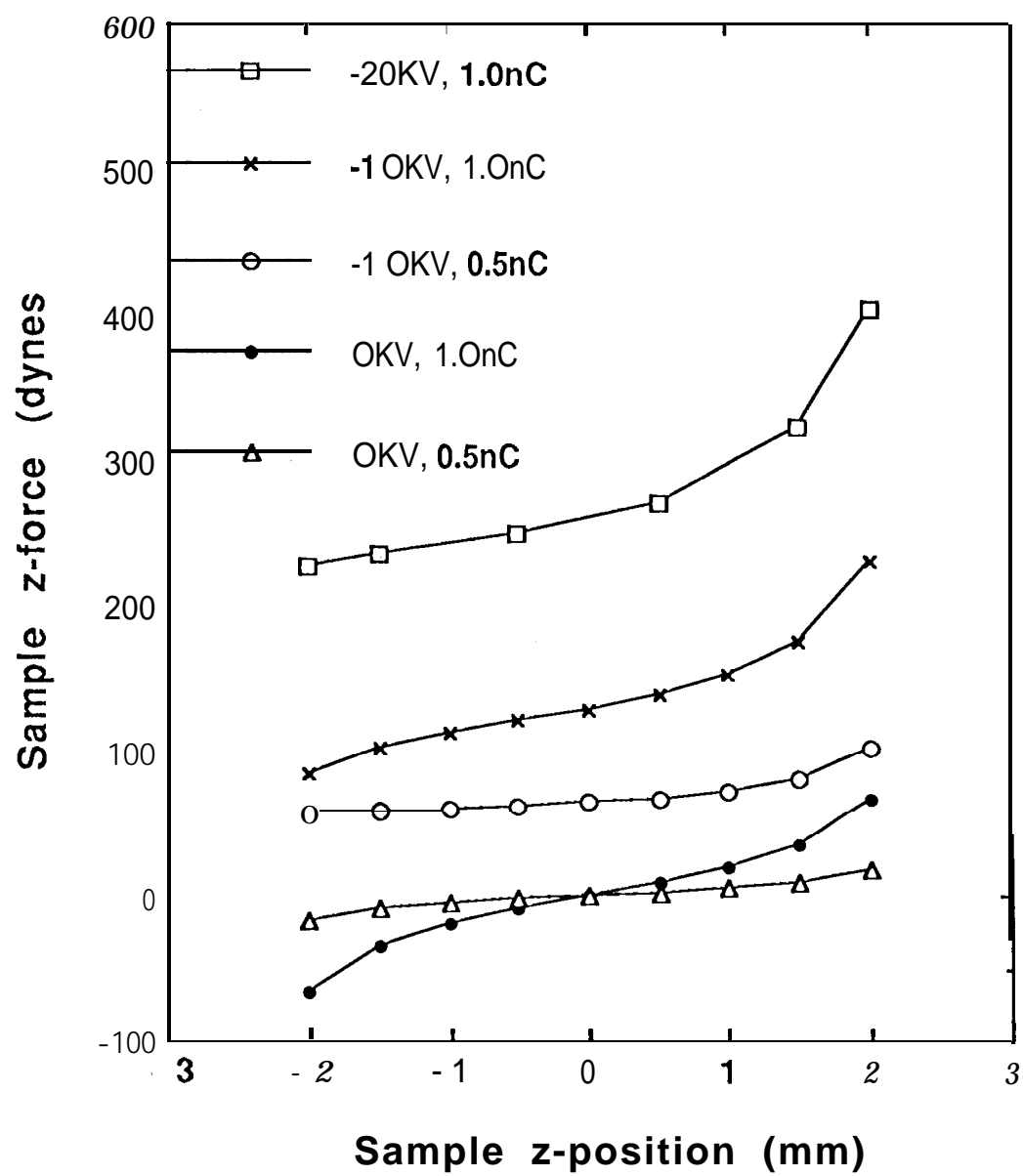


Fig. 8

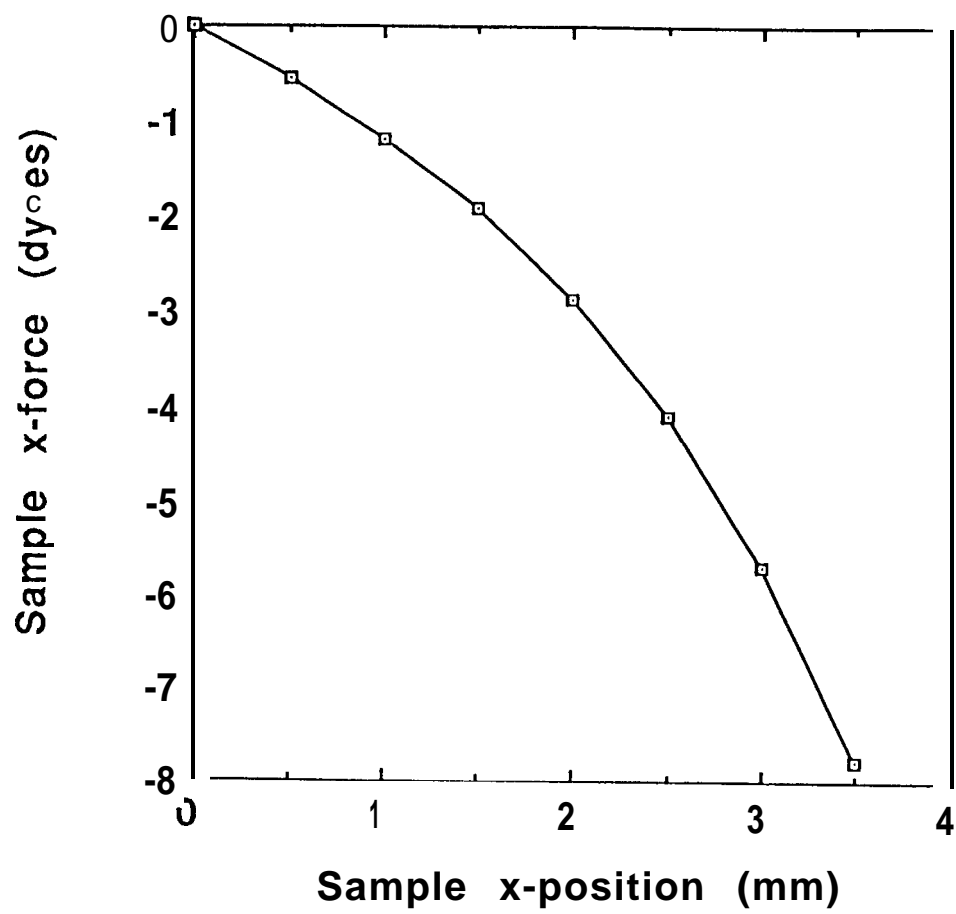


Fig. 9

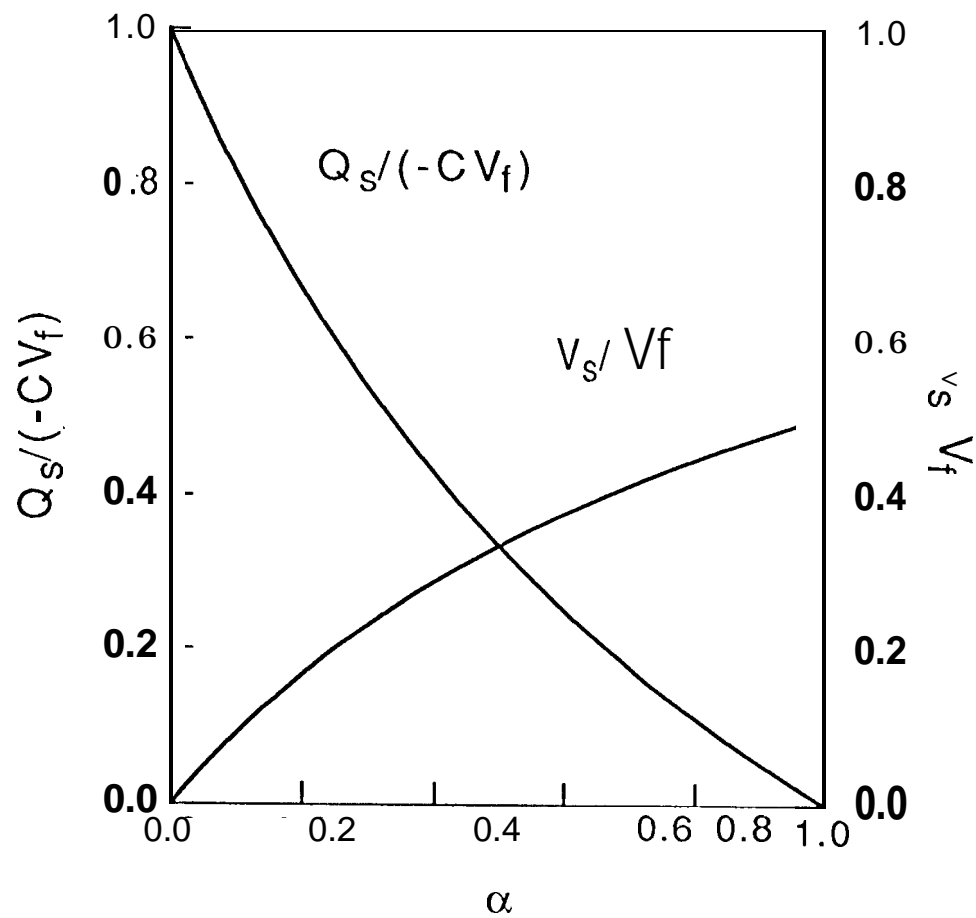


Fig. 10

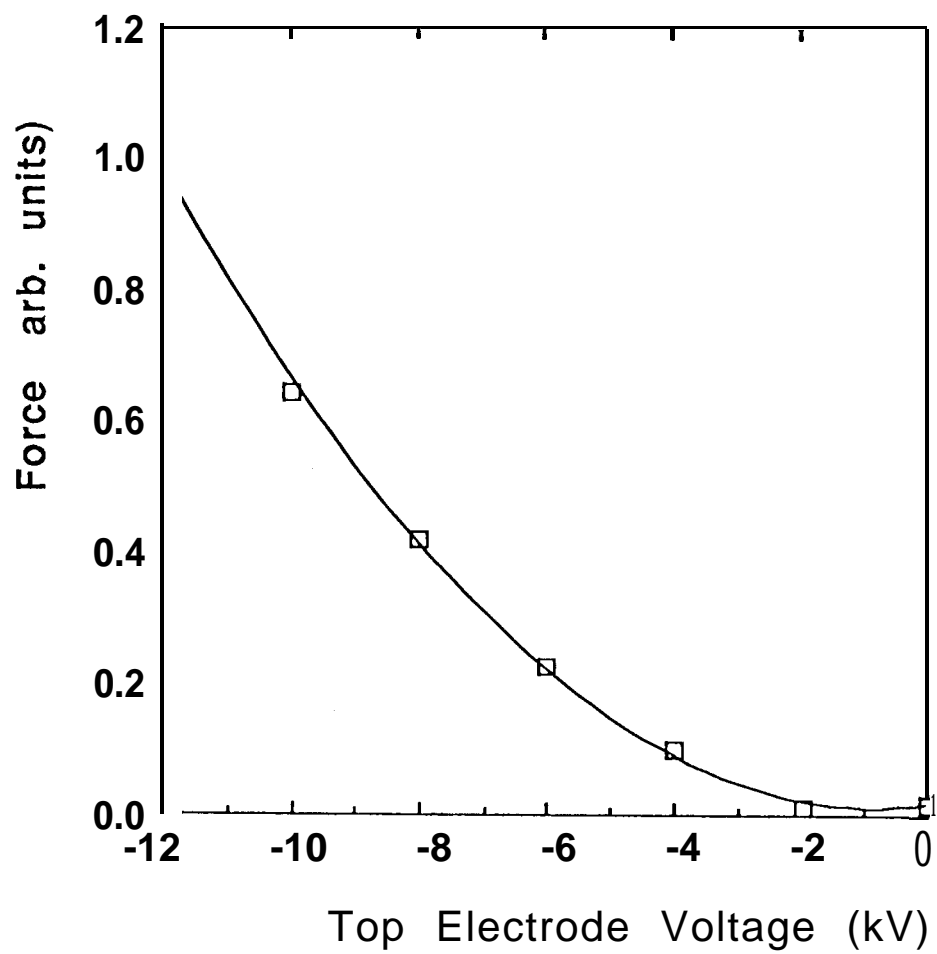


Fig. 11

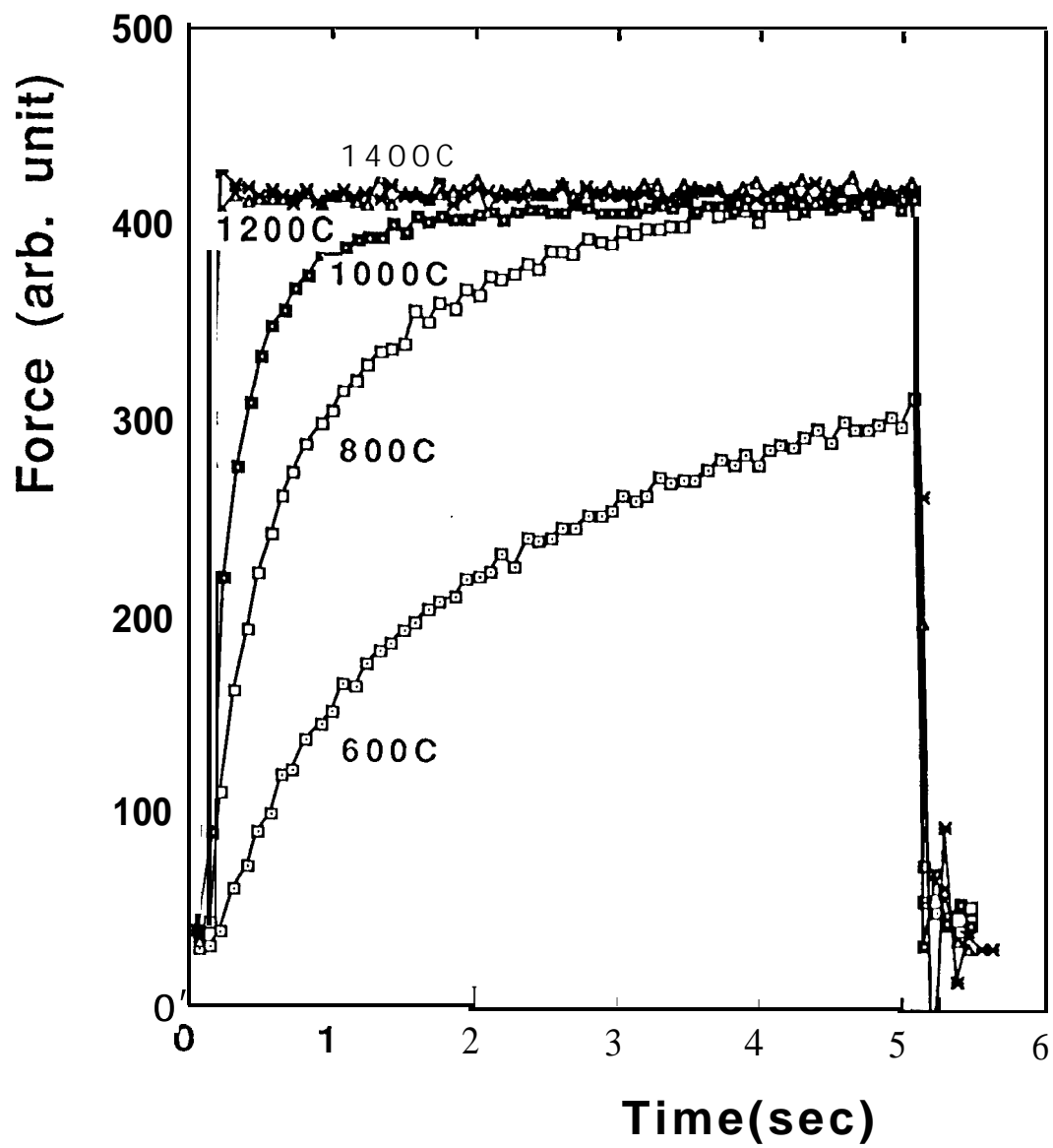


Fig. 12

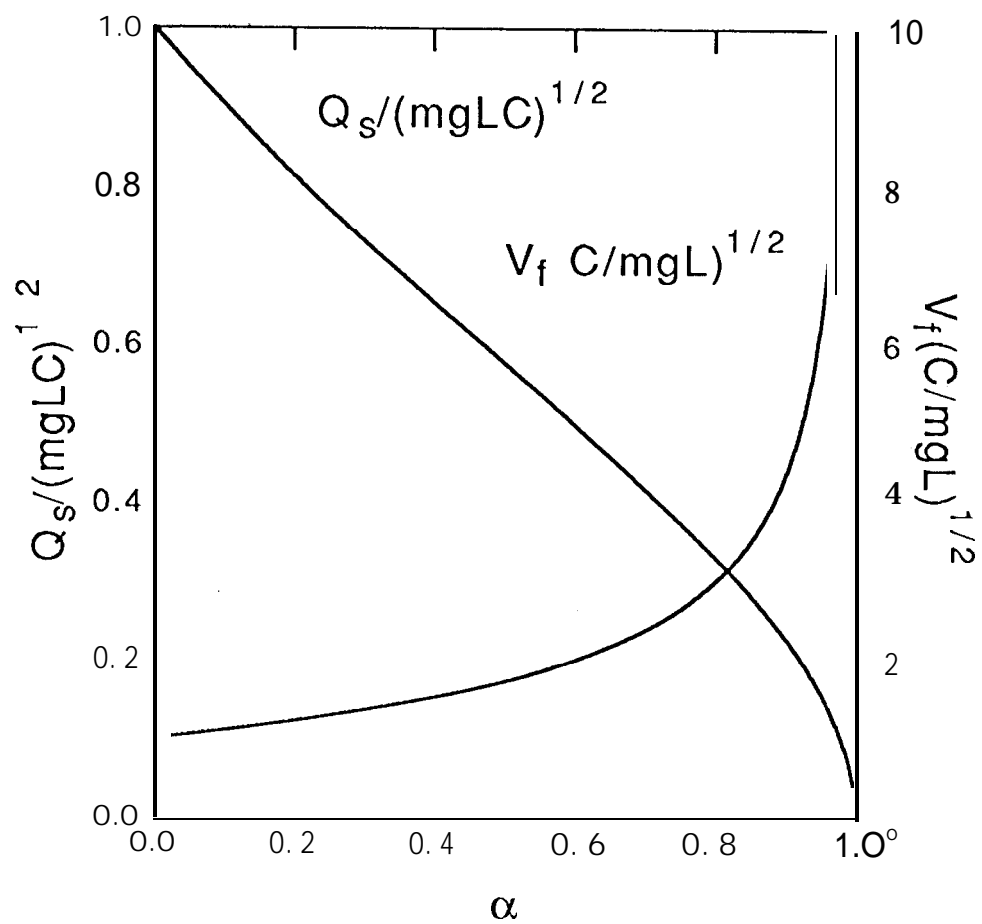


Fig. 13

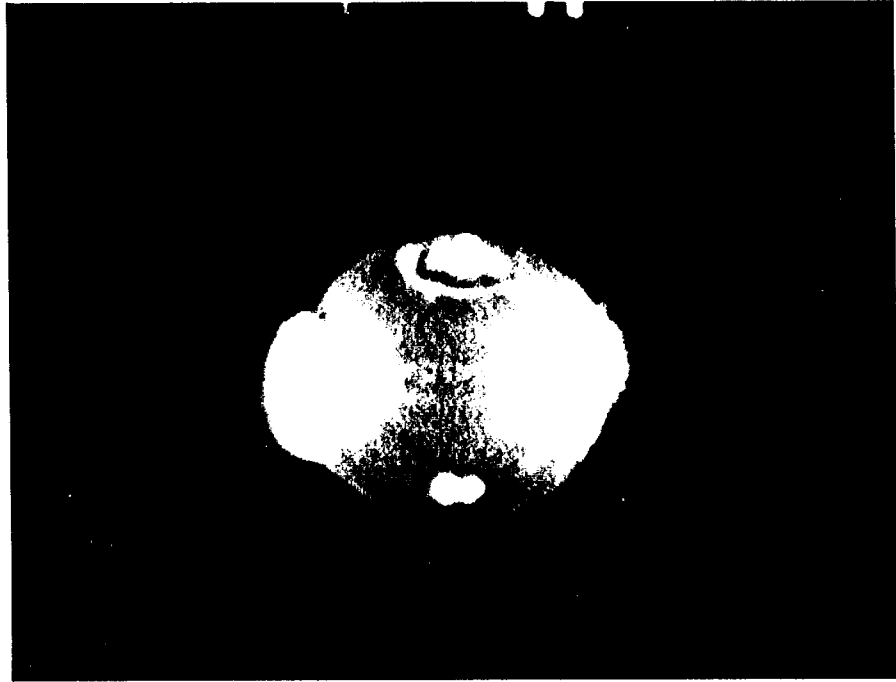


Fig. 14
Rhim et al

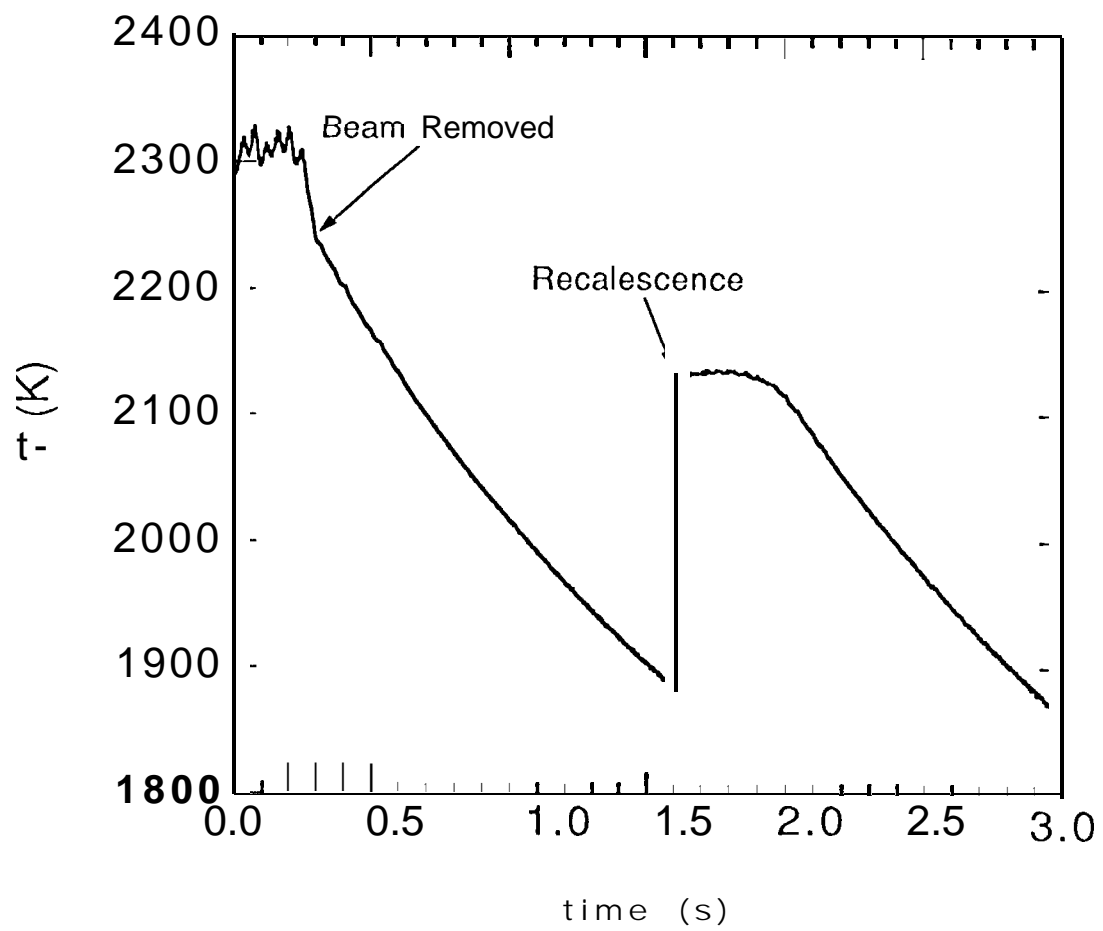


Fig. 15

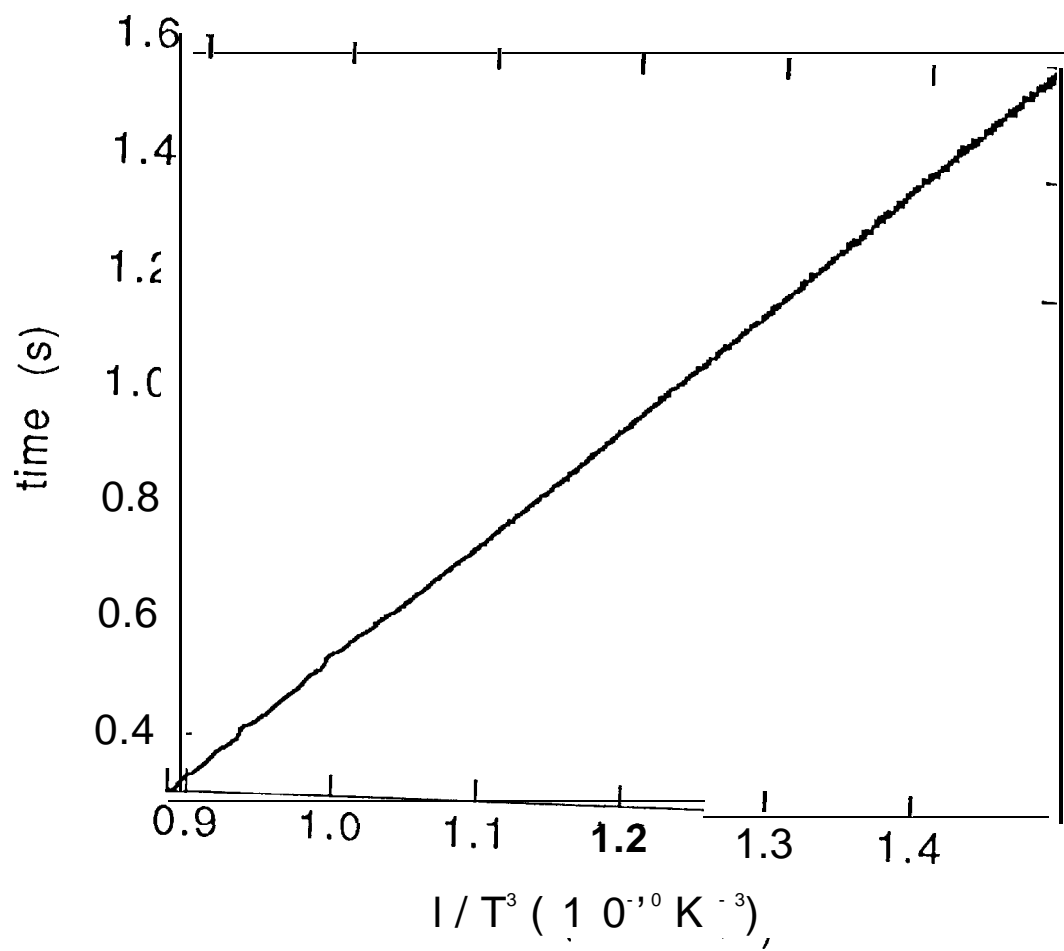


Fig. 16.